Electrically Driven, Optically Levitated Micro-Gyroscopes

Alexander D. Rider,[1,*] Charles P. Blakemore,[1] Akio Kawasaki,[1,2] Nadav Priel,[1] Sandip Roy,[1] and Giorgio Gratta[1,2]

[1] *Department of Physics, Stanford University, Stanford, California 94305, USA*
[2] *W. W. Hansen Experimental Physics Laboratory, Stanford University, Stanford, California 94305, USA*

(Dated: December 27, 2018)

We report on the electrically-driven rotation of 2.4 μm-radius, optically levitated dielectric microspheres. Electric fields are used to apply torques to a microsphere's permanent electric dipole moment, while angular displacement of the microsphere is measured by detecting the change in polarization state of light transmitted through the microsphere. This technique enables greater control than previously achieved with purely optical means. We measure the spin-down of a microsphere released from a rotating electric field, the harmonic motion of the dipole relative to the instantaneous direction of the field, and the phase lag between the driving electric field and the dipole moment of the MS due to drag from residual gas. We also observe the gyroscopic precession of the MS when the axis of rotation of the driving field and the angular momentum of the microsphere are orthogonal. We show that these observations are in quantitative agreement with the equation of motion.

I. INTRODUCTION

The ability to manipulate microscopic objects has found important applications in science and technology. The interest in optical levitation of dielectric objects in vacuum, pioneered by Ashkin and Dziedzic [1], has grown in recent times, with applications in precision measurements [2–7], surface science [8] and quantum technology [9–17]. The suggestion was made in [1] that the rotational degrees of freedom (DOFs) of an optically levitated dielectric microsphere (MS) could be manipulated using the angular momentum in circularly polarized light. This has been realized in more recent times [18–31].

Here we present a complementary technique for manipulating the rotational DOFs of an optically levitated MS by using electric fields to apply a torque to the $|\mathbf{d}| \sim 100\ e{\cdot}\mu$m permanent electric dipole moment [4] found in 2.4 μm radius silica MSs grown using the Stöber process [32]. The orientation of the dipole moment follows the orientation of the driving field so that the angular velocity, $\boldsymbol{\omega}$, can be set in both magnitude and direction [33]. Control of the rotational DOFs is an essential feature of this work, resulting in the ability to explore the dynamics of the optical levitation system.

II. EXPERIMENTAL TECHNIQUES AND PRINCIPLES

The rotational response of a trapped MS, including an applied electric field, is described by the equation of motion:

$$\dot{\mathbf{L}} = \boldsymbol{\mathcal{T}} = \mathbf{d} \times \mathbf{E} - \frac{\beta}{I}\mathbf{L} + \boldsymbol{\mathcal{T}}_{opt}, \tag{1}$$

where, $\boldsymbol{\mathcal{T}}$ is the total torque, $\mathbf{d}$ is the electric dipole moment, $\mathbf{E}$ is the electric field, $\mathbf{L}$ is the angular momentum related to the angular velocity by $\boldsymbol{\omega} = \mathbf{L}/I$, β is the rotational damping coefficient, I is the moment of inertia, and $\boldsymbol{\mathcal{T}}_{opt}$ is the optical torque. The part of the optical torque which does not average to zero over a rotation of the MS is negligible compared to the electric torques used here [34].

The angular velocity and the rotational phase of the MS are measured optically. As the MS rotates, it couples some of the incident linearly polarized optical power, $\mathcal{P}_0$, into the cross-polarized optical power, $\mathcal{P}_\perp$, according to,

$$\mathcal{P}_\perp = \mathcal{P}_0 \sin\left(\eta/2\right)^2 \sin\phi^2, \tag{2}$$

where η is the phase retardation induced between the fast and slow axes, and ϕ is the angular displacement of the MS relative to an origin in which the fast axis of the MS is aligned with the incident polarization [35]. The $\sin\phi^2$ term implies that the phase of the MS is encoded as a modulation of $\mathcal{P}_\perp$, at twice the rotation frequency, ω.

The optical trap used here is identical to that described in [36] with the addition of polarization optics to measure the cross-polarized light, $\mathcal{P}_\perp$. One polarizing beam splitter (PBS) is inserted before the trap to define the linear polarization of the incident light, and a second PBS is placed after the trap to extract $\mathcal{P}_\perp$ and measure the rotational phase of the MS. The remainder of the optical system, described in [36], is capable of stabilizing the optical trap at high vacuum.

A vacuum system is used to control and measure the residual gas pressure between 2×10^{-6} mbar and 0.1 mbar for the measurements described below. The vacuum pressure is tuned by introducing or removing N_2 gas and is measured by a cold-cathode gauge for pressures up to 10^{-4} mbar, a capacitance manometer for pressures between 10^{-4} and 10^{-2} mbar, and a Pirani gauge for pressures between 10^{-3} and 1 mbar. The cold cathode gauge is found to affect the charge the MS, so it is only used to measure the 2×10^{-6} mbar base pressure of the vacuum system after an experimental run. The capacitance manometer does not cover the full range of vacuum pressures used, so the Pirani gauge is calibrated against

* arider@stanford.edu

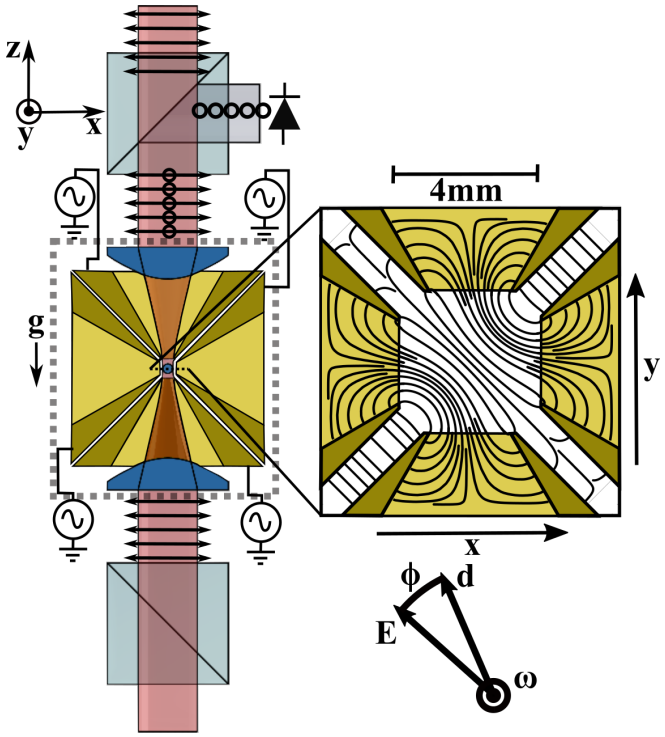

FIG. 1. Cross-section of the electrodes and polarization optics used in this work. The MS is levitated by an optical system identical to that described in [36], with the addition of the polarization optics used to measure the rotational state of the MS. The dashed lines denote the components inside the vacuum chamber. The voltages on each of the six electrodes around the trapping region are driven to exert arbitrary torques on the MS's permanent dipole moment. To demonstrate how the electrodes are used to generate arbitrary fields at the center of the trap, the detail to the right shows a slice of the electric field streamlines calculated by FEA. The electrodes on the top and on the left are at $+V$, while those on the bottom and on the right are at $-V$. Note that the left side of the figure represents a vertical cross-section. The convention used to define ϕ is also illustrated to the bottom right.

the more accurate capacitance manometer, where there is overlap. This system is capable of measuring the pressure to an accuracy of 10% for N_2 over the range of interest [37].

The trapping region of the apparatus is schematically illustrated in Fig. 1, which shows a cross-section of the pyramidal electrodes used to apply torquing electric fields to the MS. The six electrodes define a cubic trapping cavity 4 mm on a side. Each electrode is connected to a high-bandwidth, high-voltage amplifier driven by a digitally synthesized analog signal. This apparatus is capable of producing arbitrary three-dimensional electric fields up to 100 kV/m in magnitude at frequencies as high as 150 kHz. To produce a spinning electric field, a sinusoidal voltage is applied to a set of four electrodes in a plane, with a phase offset of $\pi/2$ between successive electrodes. A finite element analysis (FEA) is used to calculate the electric field produced by this electrode geometry. It is found that the x component of the field in the center of the trap, E_x, is well approximated by $E_x = 0.66(\Delta V_x/\Delta x)$, where ΔV_x is the potential difference across a pair of electrodes, and $\Delta x = 4$ mm is the electrode separation. The same statement applies to E_y and E_z.

Before performing a measurement, the MS is discharged as described in [3, 8, 38]. In addition, the MS is prepared in a state of known angular momentum and rotational phase by dissipating any initial angular velocity using 0.1 mbar of N_2 gas. An electric field rotating at $\omega_0 = 2\pi\cdot(1\text{ Hz})$ with $E = 41$ kV/m is then turned on to align $\mathbf{d}$ with $\mathbf{E}$. The chamber pressure is reduced to the base pressure of the vacuum system and ω_0 is increased at a rate of 100 Hz/s to the desired final rotation frequency. Changes in the rotational dynamics in response to changes in the electric field magnitude and direction, as well as the damping coefficient, β, can then be observed. The data presented here were collected with one specific MS. However, similar behavior is observed with other MSs, once d and I are measured.

III. OBSERVATIONS AND DYNAMICS

A typical amplitude spectrum of $\mathcal{P}_\perp$, in the region around twice the drive frequency, with $\omega = 2\pi\cdot(50\text{ kHz})$ is shown in the top panel of Fig. 2. A clear peak which follows the frequency, ω_0, of the electric driving signal is observed at $2\omega_0$. The ∼10 ppm amplitude modulation caused by rotation of the MS implies that the relative phase retardation of this MS is $\eta \sim 10^{-2}$. The prominent sidebands are caused by harmonic oscillation of the

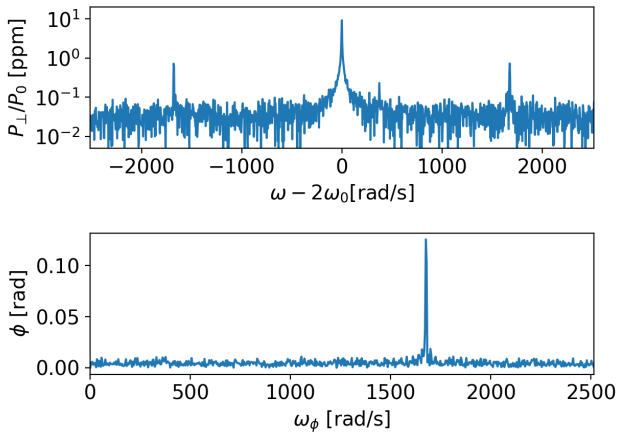

FIG. 2. Top: typical amplitude spectrum of $P_\perp$ for a MS prepared in a state of angular momentum pointing along the $\hat{\mathbf{z}}$ direction. The MS is spinning with $\omega_0 = 2\pi\cdot(50\text{ kHz})$, driven by an electric field with $E = 27$ kV/m. The prominent line with sidebands are universal signatures of the MS rotation, with the position of the central line following the drive frequency. The sidebands are caused by phase modulation of the rotation frequency, as shown in the bottom panel.

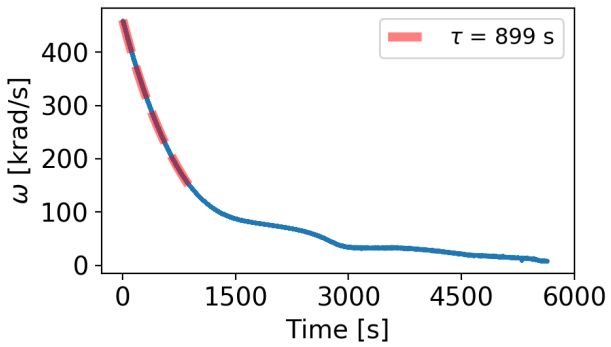

FIG. 3. Time evolution of ω after the driving electric field is switched off. For $\omega \gtrsim 150$ krad/s the angular velocity exhibits an exponential decay. For $\omega \lesssim 150$ krad/s the dynamics are modified by a torque that could be explained by a ∼100 ppm degree of ellipticity in the 1 mW trapping beam and the $\eta \sim 10^{-2}$ phase retardation of the MS.

dipole about the (rotating) direction of the electric field, which can be seen by demodulating the phase of $\mathcal{P}_\perp$ relative to the electric field carrier signal as shown in the bottom panel of Fig. 2.

After initializing the MS with a definite angular momentum and phase, the conditions can be changed to observe different solutions of the equation of motion. The simplest solution occurs when the drive electric field is switched off, so that only the drag term, $-(\beta/I)\mathbf{L}$, remains in Eq. 1 and the initial angular momentum decays according to:

$$\mathbf{L}(t) = e^{-t/\tau}\mathbf{L}(0). \tag{3}$$

Here, the damping time τ, is related to the damping coefficient by $\tau = I/\beta$. This decay is illustrated in Fig. 3 at the base pressure of the vacuum system (2×10^{-6} mbar). For the first 1000 s, $\omega \gtrsim 150$ krad/s, the drag torque dominates, and the data are well modeled by an exponential decay. As the angular velocity decreases, other torques become more important. The additional torque required to explain the slower decline in angular velocity is $\boldsymbol{\mathcal{T}}' \sim 10^{-23}$ N·m. This torque could be explained by, e.g., a ∼100 ppm ellipticity in the 1 mW trapping beam and the observed MS phase retardation, $\eta \sim 10^{-2}$ [34, 39].

The simplest dynamics with the electric dipole interacting with a rotating electric field can be analyzed in the case where the electric field is rotating about a fixed axis with the dipole lying in the same plane as the electric field. In the frame co-rotating with $\mathbf{E}$, Eq. 1 reduces to an equation of motion for ϕ, the angle between the electric field and the dipole,

$$\ddot{\phi} = -\omega_0\Omega\sin(\phi) - \frac{1}{\tau}(\omega_0 + \dot{\phi}), \tag{4}$$

where,

$$\Omega \equiv d\,E/(I\omega_0). \tag{5}$$

For sufficiently low damping, $\tau\Omega > 1$, this equation has an equilibrium solution,

$$\phi_{eq} = -\arcsin\left(\frac{1}{\tau\Omega}\right) = -\arcsin\left(\frac{\beta\omega_0}{d\,E}\right), \tag{6}$$

and can be linearized to give harmonic oscillation at the frequency

$$\omega_\phi = \sqrt{\cos(\phi_{eq})\omega_0\Omega} = \sqrt{\cos(\phi_{eq})\frac{E{\cdot}d}{I}}. \tag{7}$$

This results in the sidebands shown in Fig. 2. The dependence of ω_ϕ on the magnitude of the driving electric field, E, is well-modeled by Eq. 7, as shown in Fig. 4. The equilibrium phase lag ϕ_{eq} may be neglected because $\tau\Omega \gg 1$ at the base presssure of the vacuum system. The fit shown in Fig. 4 extracts the ratio (d/I), which can be used to determine the dipole moment, d, if the MS is assumed to be a uniform sphere with the radius, $r_{MS} = 2.40 \pm 0.02$ μm and mass $M_{MS} = 85 \pm 9$ pg, measured for this lot of MS in Ref. [40]. This procedure gives $I = (2.0 \pm 0.2)\times10^{-25}$ kg·m^2, which implies $d = 135 \pm 14$ $e{\cdot}\mu$m, in agreement with the measurements reported in [4].

The equilibrium phase lag ϕ_{eq} between $\mathbf{d}$ and $\mathbf{E}$ is expected to increase with the pressure P, as the drag from the gas increases. In the molecular flow regime, the damping coefficient, β, can be written as $\beta = k{\cdot}P$, where k is a constant that depends on the geometry of the MS, as well as the temperature and species of residual gas [41, 42]. The argument to the arcsin in Eq. 6 can then be parameterized by

$$\frac{\omega_0\beta}{d\,E} = \frac{\omega_0 k}{d\,E}{\cdot}P = \frac{P}{P_{\pi/2}}, \tag{8}$$

where $P_{\pi/2} \equiv d\,E/(\omega_0 k)$ is the pressure at which $\phi_{eq} \to -\pi/2$, where the MS rotation loses lock with the driving

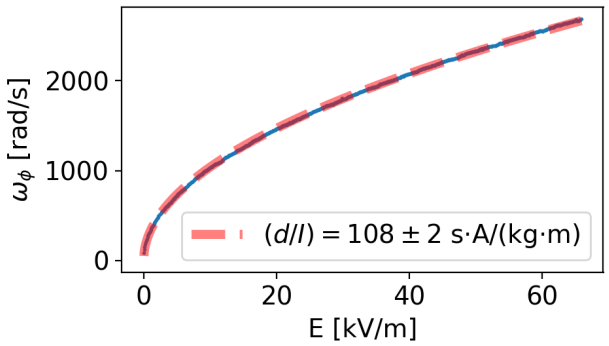

FIG. 4. Harmonic oscillation frequency, ω_ϕ, versus driving electric field amplitude, E, for a MS spinning at $\omega_0 = 2\pi{\cdot}(50$ kHz) at a pressure of 2×10^{-6} mbar. The data is fit to Eq. 7, obtaining $(d/I) = 108 \pm 2$ s·A/(kg·m) and $d = 135 \pm 14$ $e{\cdot}\mu$m (see text).

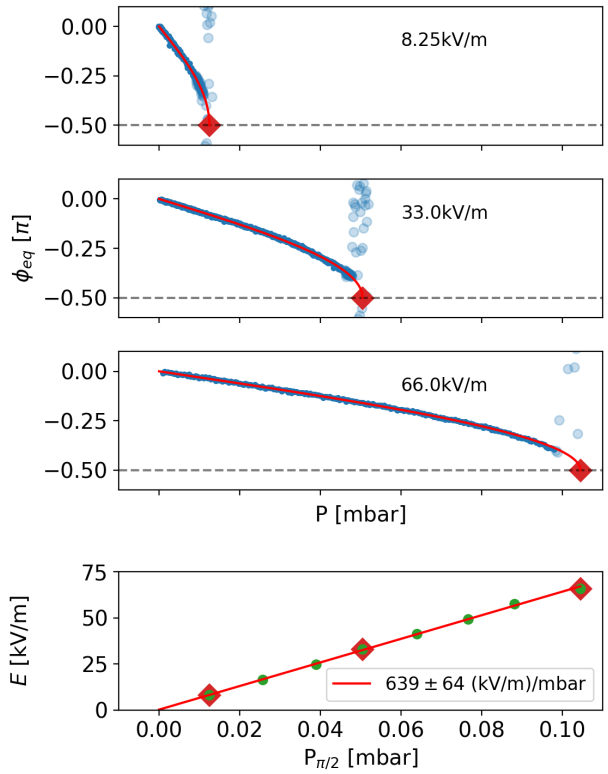

FIG. 5. Top three panels: Equilibrium phase, ϕ_{eq}, versus chamber pressure for several magnitudes, E, of the driving field with $\omega_0 = 2\pi\cdot(50\text{ kHz})$. For each value of E, ϕ_{eq} increases until the MS loses lock with the field, and the phase becomes random. For each E, a fit to Eq. 6 (with the argument as in Eq. 8) is shown in red. $P_{\pi/2}$ is identified by a red diamond. Bottom panel: The linear relationship between $P_{\pi/2}$ and E, where more values of E are included. The slope of the fit of E vs p_{max} is (639 ± 64) (kV/m)/mbar. Assuming the dipole moment measured from the frequency of small oscillations, this gives $k = \beta/P = (4.4 \pm 0.7) \times 10^{-25}$ m^{3}s, which is consistent with $k = \beta/P = 3.9 \times 10^{-25}$ m^{3}s predicted by kinetic theory for a 2.4 μm radius sphere in thermal equilibrium with 300 K N_2 gas in the molecular flow regime [41, 42].

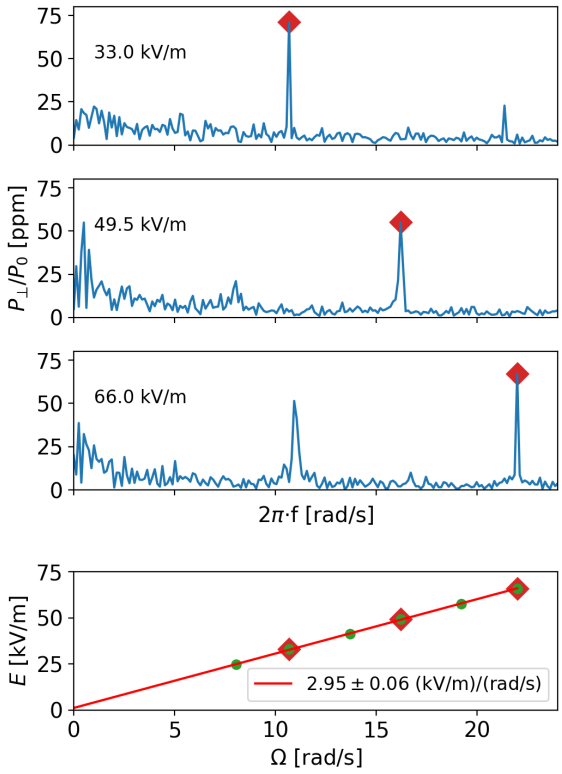

FIG. 6. Top three panels: Spectra of the cross-polarized light intensity, $\mathcal{P}_\perp$, for a MS precessing about the $\hat{\mathbf{x}}$ axis while spinning at $\omega_0 = 2\pi\cdot(50\text{ kHz})$. The modulation of the cross-polarized light occurs predominantly at twice the precession frequency denoted by red diamonds. Bottom panel: Ω for different driving fields, E. The slope of the fit function (red line) provides $(d/I) = \omega_0\Omega/E = 106 \pm 2$ s·A/kg·m, which is consistent with the measurement of d/I from the frequency of small oscillations.

electric field (in practice fluctuations cause the MS to lose lock before ϕ_{eq} reaches $-\pi/2$).

This functional behavior is apparent in the data, as shown in in the three top panels of Fig. 5 for three different amplitudes of the driving field. It is evident that the unlocking pressure depends on the field amplitude and that after losing lock ϕ_{eq} becomes random. $P_{\pi/2}$ can be extracted from a fit for each field amplitude, as plotted (for several more values of the field) in the bottom panel of Fig. 5. The linear relationship $k = d\,E/(\omega_0 P_{\pi/2})$ is evident from the data, and a fit reports the value $k = (4.4 \pm 0.7) \times 10^{-25}$ m^{3}s, assuming $d = 135 \pm 14\ e\cdot\mu$m. This is consistent with the value $k = 3.9 \times 10^{-25}$ m^{3}s predicted by the model [41, 42] for a 2.4 μm radius MS in thermal equilibrium with 300 K N_2 gas.

When the electric field rotation axis and the angular momentum are not aligned, the dynamics are complex and depend sensitively on the initial conditions. For $\Omega \ll \omega_0$, and a field $\mathbf{E}(t) = E\cdot(\cos(\omega_0 t)\hat{\mathbf{z}} - \sin(\omega_0 t)\hat{\mathbf{y}})$, rotating about the $\hat{\mathbf{x}}$ axis, an approximate solution is given by,

$$\mathbf{L}(t) = L\cdot\{\cos[(\Omega/2)t]\,\hat{\mathbf{z}} + \sin[(\Omega/2)t]\,\hat{\mathbf{y}}\} \tag{9}$$

and,

$$\begin{aligned}\mathbf{d}(t) = -d\cdot\Big\{&\cos[\omega_0(\Omega/2)t]\ \hat{\mathbf{x}} \\ &+ \sin[(\omega_0 + \Omega/2)\,t]\cos[(\Omega/2)t]\ \hat{\mathbf{y}} \\ &+ \sin(\Omega/2)\ \hat{\mathbf{z}}\Big\},\end{aligned} \tag{10}$$

in the absence of dissipation.

In this case, the angular momentum vector $\mathbf{L}$, undergoes retrograde precession, with respect to the right hand rule, about the axis of rotation of the electric field at angular frequency $\Omega/2$. This behavior is observed as a low-frequency modulation of the cross-polarized light most prominently at Ω, twice the precession frequency. The

amplitude spectra for a precessing MS driven by a range of electric fields magnitudes are shown in Fig. 6, in which the MS is spinning at $\omega_0 = 2\pi\cdot(50\text{ kHz})$. As expected, the precession frequency is proportional to the magnitude of the driving electric field. The slope of Ω vs E is consistent with the previous determination of (d/I) from the harmonic oscillation about a rotating field. This measurement takes advantage of the unique ability to apply torques about an arbitrary axis using electric fields.

IV. CONCLUSIONS

We have demonstrated a technique capable of manipulating and measuring the rotational degrees of freedom of an optically levitated MS using a rotating electric field as the drive and polarized light for the readout. Electrically-driven rotation has several advantages over previous work, in which the rotation was driven with circularly polarized light. The drive mechanism is provided by simple electronics, eliminating interference with the optical readout. The MS can be rotated about an arbitrary axis, independently from the configuration of the trapping laser beam(s). The rotational frequency and phase of the MS can be fully controlled, expanding the range of possible measurements, including those where phase control is important. For instance, once the dipole moment of a MS is measured, from the frequency of small oscillations that the dipole undergoes with respect to the direction of the driving field, the residual gas pressure in the immediate vicinity of the MS can be measured by the phase shift between the MS rotation and the driving field.

This work has several potential applications. Electrically rotated, optically levitated MSs could be used as micro-gyroscopes. The small oscillation of the dipole in the rotating reference frame of the electric field is a low dissipation DOF that could be exploited for precision measurement and cooling. In sensitive force measurements, where the electric dipole moment of the MSs may result in background forces, the rotation induced about an appropriate axis can be used to measure dipole interactions. Dipole background forces can then be distinguished from other forces of interest, and or averaged out.

MSs made from materials with larger dipole moments, such as barium titanate, could be combined with larger electric fields in order to make oscillators with natural frequencies that can be tuned over many orders of magnitude.

V. ACKNOWLEDGEMENTS

We would like to thank J. Fox (Stanford) for discussions on the readout electronics, R.G. DeVoe and A. Fieguth (Stanford) for carefully reading this manuscript, and the Moore group (Yale) for general discussions related to trapping microspheres. This work was supported, in part, by NSF grants PHY1502156 and PHY1802952, ONR grant N00014-18-1-2409 and the Heising-Simons Foundation. AK acknowledges the partial support of a William M. and Jane D. Fairbank Postdoctoral fellowship of Stanford University. NP acknowledges the partial support of the Koret Foundation. Microsphere characterization was performed at the Stanford Nano Shared Facilities (SNSF), which is supported by the National Science Foundation as part of the National Nanotechnology Coordinated Infrastructure under award ECCS-1542152.

[1] A. Ashkin, Phys. Rev. Lett. **24**, 156 (1970).
[2] A. A. Geraci, S. B. Papp, and J. Kitching, Phys. Rev. Lett. **105**, 101101 (2010).
[3] D. C. Moore, A. D. Rider, and G. Gratta, Phys. Rev. Lett. **113**, 251801 (2014).
[4] A. D. Rider, D. C. Moore, C. P. Blakemore, M. Louis, M. Lu, and G. Gratta, Phys. Rev. Lett. **117**, 101101 (2016).
[5] G. Ranjit, M. Cunningham, K. Casey, and A. A. Geraci, Phys. Rev. A **93**, 053801 (2016).
[6] A. Arvanitaki and A. A. Geraci, Phys. Rev. Lett. **110**, 071105 (2013).
[7] D. Goldwater, B. A. Stickler, K. Hornberger, and J. Millen, "Levitated electromechanics: all-electrical cooling of charged nano- and micro-particles," (2018), arXiv:1802.05928.
[8] C. P. Blakemore, A. D. Rider, S. Roy, Q. Wang, A. Kawasaki, and G. Gratta, (2018), arXiv:1810.05779 [physics.ins-det].
[9] T. Li, S. Kheifets, and M. G. Raizen, Nat. Phys. **7**, 527 (2011).
[10] D. E. Chang, C. A. Regal, S. B. Papp, D. J. Wilson, J. Ye, O. Painter, H. J. Kimble, and P. Zoller, Proc. Nat. Acad. Sci. USA **107**, 1005 (2010).
[11] O. Romero-Isart, A. C. Pflanzer, F. Blaser, R. Kaltenbaek, N. Kiesel, M. Aspelmeyer, and J. I. Cirac, Phys. Rev. Lett. **107**, 020405 (2011).
[12] O. Romero-Isart, Phys. Rev. A **84**, 052121 (2011).
[13] J. Millen, P. Z. G. Fonseca, T. Mavrogordatos, T. S. Monteiro, and P. F. Barker, Phys. Rev. Lett. **114**, 123602 (2015).
[14] P. Z. G. Fonseca, E. B. Aranas, J. Millen, T. S. Monteiro, and P. F. Barker, Phys. Rev. Lett. **117**, 173602 (2016).
[15] B. R. Slezak, C. W. Lewandowski, J.-F. Hsu, and B. D'Urso, (2018), 10.1088/1367-2630/aacac1, arXiv:1802.03424.
[16] V. Jain, J. Gieseler, C. Moritz, C. Dellago, R. Quidant, and L. Novotny, Phys. Rev. Lett. **116**, 243601 (2016).
[17] A. T. M. A. Rahman and P. F. Barker, Nature Photonics **11**, 634 (2017).
[18] J. Ahn, Z. Xu, J. Bang, Y.-H. Deng, T. M. Hoang, Q. Han, R.-M. Ma, and T. Li, Phys. Rev. Lett. **121**, 033603 (2018).

[19] F. Monteiro, S. Ghosh, E. C. van Assendelft, and D. C. Moore, Phys. Rev. **A97**, 051802 (2018), arXiv:1803.04297 [physics.optics].

[20] R. Reimann, M. Doderer, E. Hebestreit, R. Diehl, M. Frimmer, D. Windey, F. Tebbenjohanns, and L. Novotny, Phys. Rev. Lett. **121**, 033602 (2018).

[21] S. Kuhn, A. Kosloff, B. A. Stickler, F. Patolsky, K. Hornberger, M. Arndt, and J. Millen, Optica **4**, 356 (2017).

[22] Y. Arita, A. W. McKinley, M. Mazilu, H. Rubinsztein-Dunlop, and K. Dholakia, Analytical Chemistry **83**, 8855 (2011).

[23] Y. Arita, E. M. Wright, and K. Dholakia, Optica **5**, 910 (2018).

[24] Y. Arita, M. Mazilu, and K. Dholakia, Nature Communications **4**, 2374 EP (2013).

[25] H. He, M. E. J. Friese, N. R. Heckenberg, and H. Rubinsztein-Dunlop, Phys. Rev. Lett. **75**, 826 (1995).

[26] A. I. Bishop, T. A. Nieminen, N. R. Heckenberg, and H. Rubinsztein-Dunlop, Phys. Rev. Lett. **92**, 198104 (2004).

[27] J. S. Bennett, L. J. Gibson, R. M. Kelly, E. Brousse, B. Baudisch, D. Preece, T. A. Nieminen, T. Nicholson, N. R. Heckenberg, and H. Rubinsztein-Dunlop, Scientific Reports **3**, 1759 EP (2013).

[28] T. M. Hoang, Y. Ma, J. Ahn, J. Bang, F. Robicheaux, Z.-Q. Yin, and T. Li, Phys. Rev. Lett. **117**, 123604 (2016).

[29] M. Mazilu, Y. Arita, T. Vettenburg, J. M. Auñón, E. M. Wright, and K. Dholakia, Phys. Rev. A **94**, 053821 (2016).

[30] W. Li, N. Li, Y. Shen, Z. Fu, H. Su, and H. Hu, Appl. Opt. **57**, 823 (2018).

[31] M. Rashid, M. Toroš, A. Setter, and H. Ulbricht, Phys. Rev. Lett. **121**, 253601 (2018).

[32] W. Stber, A. Fink, and E. Bohn, Journal of Colloid and Interface Science **26**, 62 (1968).

[33] P. Nagornykh, J. E. Coppock, J. P. J. Murphy, and B. E. Kane, Phys. Rev. B **96**, 035402 (2017).

[34] M. E. J. Friese, T. A. Nieminen, N. R. Heckenberg, and H. Rubinsztein-Dunlop, Nature **394**, 348 EP (1998).

[35] R. C. Jones, J. Opt. Soc. Am. **31**, 488 (1941).

[36] A. D. Rider, C. P. Blakemore, G. Gratta, and D. C. Moore, Phys. Rev. A **97**, 013842 (2018).

[37] Kurt Lesker, `https://www.lesker.com/newweb/gauges/convection_kjlc_2.cfm`, accessed: 2018-12-19.

[38] M. Frimmer, K. Luszcz, S. Ferreiro, V. Jain, E. Hebestreit, and L. Novotny, Phys. Rev. A **95**, 061801 (2017).

[39] A. La Porta and M. D. Wang, Phys. Rev. Lett. **92**, 190801 (2004).

[40] C. P. Blakemore, A. D. Rider, S. Roy, A. Kawasaki, P. Nadav, and G. Gratta, (To be published).

[41] A. Cavalleri, G. Ciani, R. Dolesi, M. Hueller, D. Nicolodi, D. Tombolato, S. Vitale, P. Wass, and W. Weber, Physics Letters A **374**, 3365 (2010).

[42] L. Martinetz, K. Hornberger, and B. A. Stickler, Phys. Rev. E **97**, 052112 (2018).